EIS study of the development of passive layers on Ferrous Shape Memory Alloys in alkaline conditions

ABSTRACT

This work evaluates the corrosion behavior of two iron-based shape memory alloys (Fe-28Mn-6Si-5Cr and Fe-17Mn-10Cr-5Si-4Ni-1(V,C)) in simulated concrete pore environments. The study focuses on the spontaneous passivation process under different pH conditions (13, 12, and 11) and the influence of alloy composition and mechanical pre-straining. Electrochemical techniques, including Open Circuit Potential (OCP) monitoring and Electrochemical Impedance Spectroscopy (EIS), were used to characterize the formation and stability of passive films. Equivalent electrical circuits were employed to model the evolution of the oxide layer over time. Results confirm that all materials form stable passive layers at pH 13 and 12, although different kinetics were observed depending on the alloy and mechanical condition. At pH 11, lower impedance values and minimal evolution were recorded, indicating a reduced protective effect of the passive films. The influence of Cr and Mn content, as well as mechanical pre-straining, was found to significantly affect the passivation behavior of the studied alloys.

KEYWORDS

Shape memory alloy, oxide film, corrosion resistance, aggressive ions, pitting corrosion.

1. INTRODUCTION

Shape Memory Alloys (SMAs) are a class of smart materials capable of recovering their original shape after plastic deformation when exposed to an external stimulus, typically temperature [1]. Among the different SMA families, Cu-based, Mn-based and Ti-based alloys are the most widely known. NiTiNOL, a Ti-based SMA, is the most extensively studied system; however, its relatively low yield strength, limited Young's modulus and high cost restrict its use in large-scale engineering applications.

In 1982, a new type of Fe-based SMA, commonly referred to as Shape Memory Steel (SMS), was developed [2]. In these alloys, the shape memory effect is associated with the reversible transformation between γ-austenite (fcc), the parent phase, and ε-martensite (hcp), the secondary phase. The stress-induced γ → ε transformation can be reversed by heating, enabling the material to recover its original shape. Several families of SMS have been reported, including Fe-Pt, Fe-Pd, Fe-Ni-Co and Fe-Mn-Si alloys, the latter being the group investigated in the present work. Compared with conventional SMAs, Fe-Mn-Si SMS combine the shape memory effect with the mechanical strength and versatility of steels, showing yield strengths between 200 and 1000 MPa, a Young's modulus close to 140 GPa and relatively low material cost [3–5].

Due to these characteristics, SMS have attracted increasing attention for engineering applications, which can generally be classified into actuators, where free deformation occurs, and stress-generating elements, where deformation is constrained. Typical actuator applications include seismic dampers for structural vibration control [6]. When deformation is restricted, SMS can act as stress applicators, as demonstrated in railway fishplates [7], pipe couplings [8–10] and prestressing systems. In civil engineering, Fe-Mn-Si SMS are particularly promising as prestressed reinforcement for concrete structures [4]. In this approach, prestressed SMS elements are embedded in concrete and subsequently heated after curing to induce the ε → γ transformation [10]. When the material is

mechanically constrained, this transformation generates recovery stresses that are transferred to the surrounding concrete, thereby introducing prestress into the structure. This concept has enabled the development of prestressed reinforcement systems using corrugated bars as well as repair techniques based on externally applied reinforcing strips for damaged structures [11,12]. In addition to their mechanical performance, the relatively low cost of alloying elements and the possibility of activating prestress through thermal treatment without hydraulic tensioning equipment make these materials especially attractive for civil engineering applications [3,4,13,14]

Despite these advantages, the durability of SMS in service environments remains a key issue. In reinforced concrete applications, the long-term performance of these alloys is strongly influenced by their corrosion behaviour. The limited number of studies addressing the corrosion resistance of SMS indicates that although Mn plays a fundamental role in stabilizing the shape memory effect, it may also reduce corrosion resistance [15]. For this reason, alloying elements such as Ni and Cr have been incorporated into SMS compositions to improve both mechanical properties and corrosion performance [16–19]. Recent studies have also analyzed the electrochemical response and passive film formation in Fe-based shape memory alloys, highlighting the strong influence of alloy composition and surface film stability on corrosion behavior [18,19]

Previous studies have examined the corrosion behavior of shape memory steels (SMS) in acidic environments [20–22] and in chloride-containing solutions [16,23]. In acidic media, the corrosion resistance of these alloys is strongly influenced by their chemical composition: the relatively high Mn content required to enable the shape memory effect can decrease the Icorr value and shift Ecorr to more positive potentials, worsening the corrosion behavior. Whereas alloying elements such as Cr and Si play a key role in improving the electrochemical response, showing opposite response with respect to the Mn additions [15,22,24]. Under acidic conditions, SMS typically exhibit passive-to-active transitions, with passive current densities comparable to those reported for SS 304, although a higher critical anodic current is generally required to achieve passivation [22], developing a passive film that remains susceptible to localized degradation, particularly pitting corrosion and chloride attack. In solutions with neutral pH and chloride concentrations similar to seawater, Fe-Mn-Si base SMSs exhibit localized corrosion and corrosion products that form a poorly adhering oxide film, separating from the base material [23]. In other steels, Cr additions improve the material's corrosion properties, as do Ni, N, and V additions, but in this case at the expense of SME, an effect diametrically opposed to that of increasing the percentage of Mn [16,17].

However, the electrochemical response of SMS in concrete-like environments, particularly under chloride contamination, is still not fully understood [25–28], and further investigation is required [29,30]. Previous studies conducted by the authors on the same Fe-based shape memory alloys under alkaline (pH ≈ 13) and partially carbonated conditions have provided additional insight into passive film formation. Cyclic voltammetry and X-ray photoelectron spectroscopy (XPS), including high-resolution analysis, revealed that the passive layers are mainly composed of Fe-, Mn- and Cr-based oxides, with differences in thickness depending on the alloy composition and environment . Furthermore, Mott–Schottky analysis showed that these films exhibit semiconducting behaviour, with predominantly n-type response in Fe-28Mn alloys and mixed n- and p-type behaviour in Fe-17Mn alloys, associated with the coexistence of different oxide species.

In line with those previous studies, the present work analyses the kinetics of the spontaneous passivation process of two SMS alloys under simulated concrete pore solution conditions. The study aims to evaluate the durability of these materials when used as reinforcement in reinforced concrete. To better understand their behaviour in concrete-like environments, the formation and evolution of

oxide layers are investigated through Open Circuit Potential (OCP) monitoring and Electrochemical Impedance Spectroscopy (EIS).

2. EXPERIMENTAL

The materials used in this study consist of two types of SMS with different chemical compositions. These alloys were selected due to the limited commercial availability of Fe-based shape memory alloys. As the main difference in composition is the Mn percentage, the naming of the elements will be Fe-28Mn and Fe-17Mn.

The Fe-28Mn steel was acquired at Awaji Materia Co., LTD. (http://www.awaji-m.jp/english/), and the forming process carried out at Nippon Steel Corporation consisted of melting a ingot in a vacuum induction furnace and molding ingots that were hot rolled to a thickness of 16 mm after being heated to 1200 °C for 1 hour [40].

The Fe-17Mn was acquired at Re-fer AG (https://www.re-fer.eu/en/) and was produced by melting an ingot in an induction furnace without a protective atmosphere and molded in a cylindrical mold 90 mm in diameter and 300 mm in length. The ingot is heated to 1100 °C and hot-pressed to a diameter of 50 mm, followed by gradual reheating to 1100 °C for 15 minutes and hot-pressed until the final diameter of the tested bar is reached [41].

The full composition of both steels can be found on Table 1. The Fe-28Mn samples have a 32 mm diameter, a round shape, and have been pre-stressed. The Fe-17Mn is examined under two conditions: a pre-strained state (5% deformation strain), referred to as Fe-17Mn(P), and an unstrained state, referred to as Fe-17Mn(U). Both Fe-17Mn samples are acquired in the form of corrugated bars with a nominal diameter of 11 mm.

	Mn	Cr	Si	Ni	V	C
Fe-28Mn	28.40	5.20	5.70	-	-	0.02
Fe-17Mn	17.20	10.00	5.00	4.20	0.74	0.18

Table 1: Chemical composition of the studied Shape Memory Alloys.

Before the electrochemical tests, all specimens were mechanically ground to achieve a mirror-like finish using SiC papers up to 2400 grit. Then, samples were polished with diamond paste to a grain size of 1 µm.

Electrochemical measurements were conducted using an Autolab 30 Potentiostat equipped with an FRA module from EcoChemie®, utilizing a three-electrode cell with a working electrode surface area of 0.33 cm^2 and a Ti-MMOx wire as the counter electrode. The reference electrode used was a Hg/HgO 0.1 M KOH electrode, although the measurements were later referenced to a calomel electrode for clarity's sake.

The materials were submerged in NaOH 0.1M + KOH 0.1M solutions, with a pH = 13, to simulate the environment present in the concrete pores. In the lower pH experiments, the solutions were bubbled with CO_2 to generate H_2CO_3, lowering the pH value until the desired value. The pH value reading was performed with a pH 50 Vio Lab (XS instruments).

Impedance measurements were conducted between 10 kHz and 1 mHz with an AC signal amplitude of 10 mV_{rms}. The samples were maintained in the solution and monitored for 7 days, repeating the measurements every 24 hours. Between EIS measurements, the OCP was also registered.

For the process of fitting the experimental impedance data to the proposed equivalent models, the SimadV2W10 software was used, based on an optimization algorithm for minimizing a function of n variables using a simplex method in the n dimensions of a triangle to approximate an optimal mathematical form [42]. The fitting procedure minimizes the mean squared error (χ^2) between the experimental impedance values (Z_e) and the simulated values (Z_s). This calculation is iteratively performed for all frequency points (i) within the experimental frequency range (N). The expression used to evaluate the fitting error is given in Eq. *1*.

$$\chi^2 = \sum_{i=1}^{n} \left[\left(\frac{Z'_e - Z'_c}{|Z_e|} \right)^2 + \left(\frac{Z''_e - Z'_c}{|Z_e|} \right)^2 \right] \quad \text{Eq. 1}$$

3. RESULTS AND DISCUSSION

To analyse the kinetics of the spontaneous passivation process under simulated natural conditions, samples were immersed in solutions with a pH similar to that of a concrete environment. These tests aimed to evaluate the material's durability when used as reinforcement in reinforced concrete.

Figure 1 illustrates the evolution of the OCP with immersion time for the tested samples. The OCP value increases in all samples, indicating the formation of a protective oxide film. This evolution followed the expected behaviour and is consistent with what other authors have also observed it in carbon steels in alkaline solutions [26].

The passive layer forming kinetics differ depending on the type of steel. To assess the evolution of the materials, a mathematical adjustment of the observed OCP evolutions using exponential growth functions have been made [43]. For Fe-17Mn (both formats) Eq. 2 has been used, as the evolution was characterized by a single time constant.

Fe-28Mn presented two well-defined stages governed by two time constants, so Eq. 3 has been used. The parameter y_0 corresponds to the asymptotic value of the equations, t_1 and t_2 stand for the time constants and A_1 and A_2 correspond to the amplitude of the OCP evolution curve in relation with the first or second time constant. Although the use of exponential fitting to describe the evolution of the open circuit potential (OCP) is not a widely established approach in corrosion studies, it was adopted here as a practical method to estimate the stabilization time of the potential. This stabilization time was taken as an indicator of the moment at which the passive film can be considered fully developed, providing a quantitative reference for comparing the passivation kinetics of the studied alloys.

$$y = y_0 + A_1 e^{-x/t_1} \quad \text{Eq. 2}$$

$$y = y_0 + A_1 e^{-x/t_1} + A_2 e^{-x/t_2} \quad \text{Eq. 3}$$

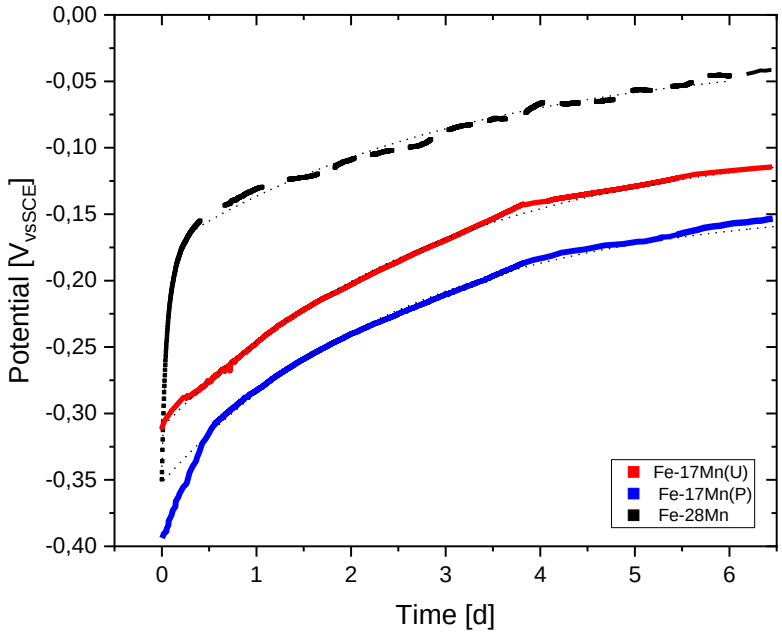


Figure 1: Evolution of the open circuit potential of the materials with the immersion time in a 0.1M NaCl + 0.1M KOH solution

The stabilization time (t_{stb}) for the passive layer was defined as the time required to reach 90% of the asymptotic value and was calculated with a cumulative distributed function (Eq. 4).

$$cdf = 1 - e^{x/t_1} = 0.9 \quad \text{Eq. 4}$$

The stabilization time was considered 2.3 times the value of the time constant (Eq. 5) for the Fe-17Mn alloys and the addition of 2.3 times both time constants (t_1 and t_2) for the Fe-28Mn. Table 2 presents the parameter for each equation, y_0, A_1, A_2, t_1, t_2 and t_{stb}, as well as the Goodness-of-Fit (R^2).

$$x = \ln(0{,}1)\, t_1 = 2{,}3 t_1 \quad \text{Eq. 5}$$

	Fe-28Mn	**Fe-17Mn(U)**	**Fe-17Mn(P)**
y_0	- 20 $mV_{vs\ SCE}$	- 92 $mV_{vs\ SCE}$	- 142 $mV_{vs\ SCE}$
A_1	- 166 $mV_{vs\ SCE}$	- 220 $mV_{vs\ SCE}$	- 210 $mV_{vs\ SCE}$
t_1	1,6 h	68,6 h	62,2 h
A_2	- 150 $mV_{vs\ SCE}$	-	-
t_2	77,3 h	-	-
R^2	0,997	0,999	0,999
t_{stb}	181,5 h	157,8 h	143,1 h

Table 2: Fitting parameters (y_0, A_1, A_2, t_1, t_2 y R^2) of the steels under study to the exponential functions shown in Figure 1, as well as the OCP stabilization times.

Figure 1 showed that the noblest values correspond to Fe-28Mn, which indicated that a more oxidized film is generated, with a greater presence of Fe^{3+} and Mn^{3+}/Mn^{4+}, a fact that is in accordance with the lower chromium content of the alloy [44].

In other studies from the group [30,44], the thickness of passive films generated by cyclic voltammetry in the Fe-28Mn are thicker than those of the Fe-17Mn. Although this passive layer has been generated by accelerated growth, it is assumed that the thickness ratio is maintained under conditions of

spontaneous passivation. The longer stabilization time for Fe-28Mn alloy can maybe be attributed to the development of thicker films.

The diagrams presented in Figure 2 show the evolution of the Fe-17Mn(U) |Z| values, with a very notable increase between day 0 and day 1 and a constant rate between days 1 and 6. Although complete stabilization is not distinguished, the passive layer is considered established after approximately 6.5 days, in accordance with the OCP data (Figure 1). The Bode diagram (Figure 2b) presents two-time constants with better definition as the immersion time increases.

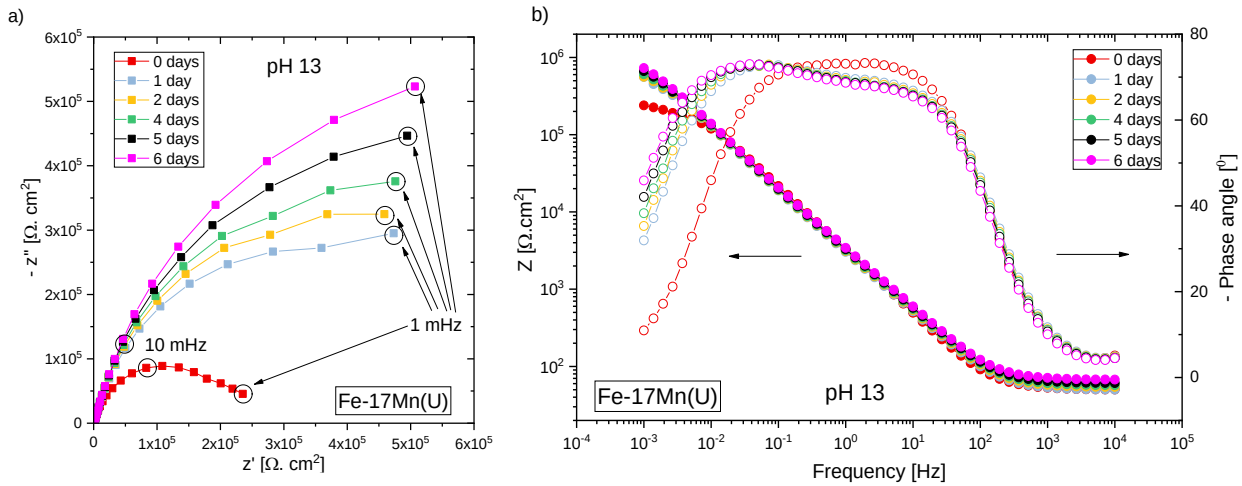


Figure 2: Evolution of the impedance values of Fe-17Mn(U) during the immersion time in a 0.1M NaOH + 0.1M KOH solution, Nyquist (a) and Bode (b) diagrams.

The evolution of |Z| in the Fe-17Mn(P), presented in Figure 3, shows a very regular evolution between day 0 and day 6, unlike Fe-17Mn(U). In correspondence with the data obtained from the OCP monitoring, the passive layer is considered stablished at the 6th day. The Bode diagram (Figure 3b) also presents two clear time constants, with a less defined third one.

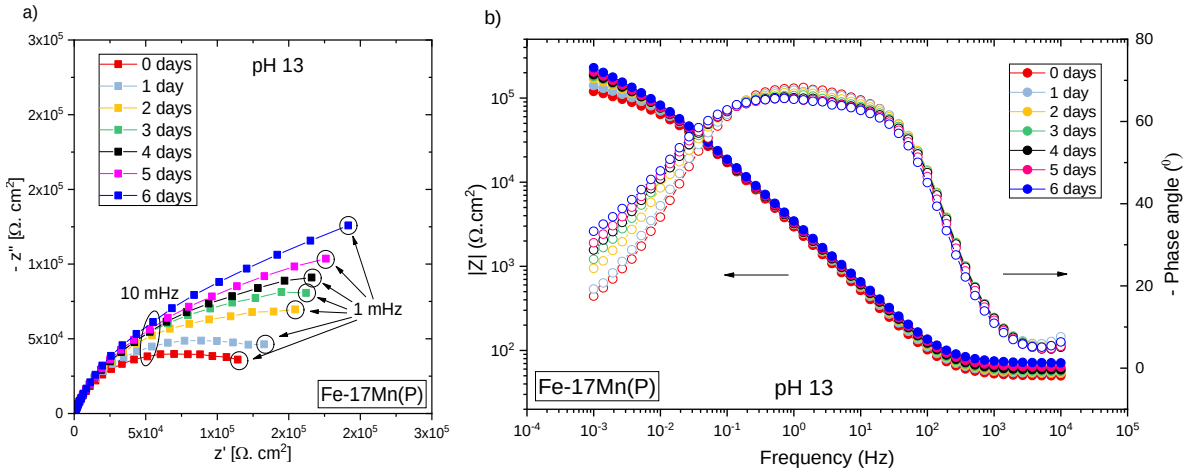


Figure 3: Evolution of the impedance values of Fe-17Mn(P) during the immersion time in a 0.1M NaOH + 0.1M KOH solution, Nyquist (a) and Bode (b) diagrams.

The evolution of the |Z| value of Fe-28Mn, presented in Figure 4 is notably different than both Fe-17Mn formats. An increase in the Z value is observed between day 0 and day 3, with a latter stabilization. The morphology of phase angle of the Bode diagram (Figure 4b) presents single wide maximum, pointing to the existence of two overlapping time constants, with a third time constant appearing at lower frequencies.

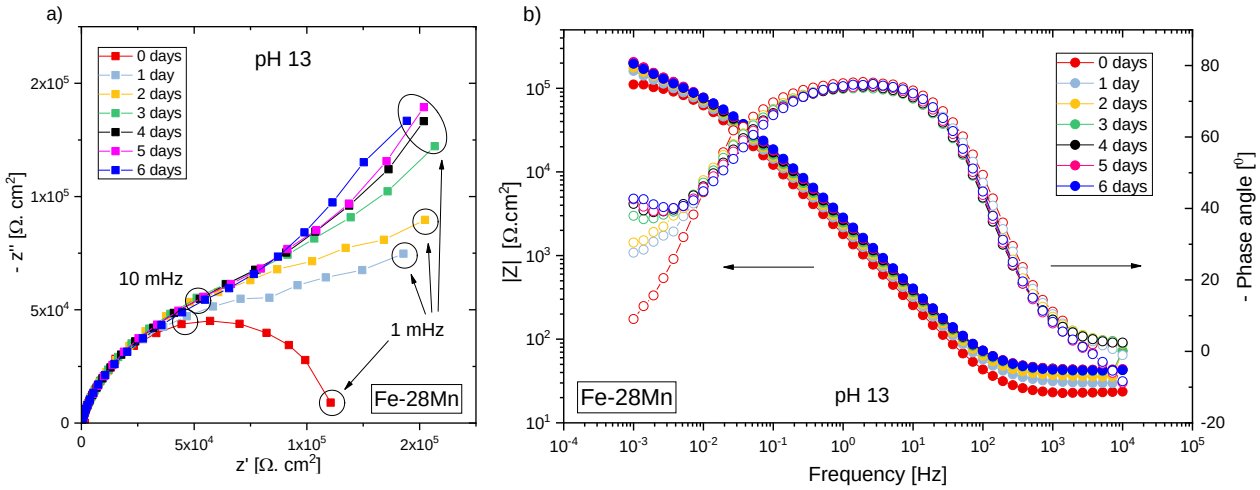


Figure 4: Evolution of the impedance value of the Fe-28Mn alloy after being immersed in the 0.1 M NaOH + 0.1 M KOH solution for 7 days, represented in the Nyquist (a) and Bode (b) diagrams.

Figure 5 compares the impedances of the steels after passive film generation, with Fe-28Mn presenting the lowest impedance value at low frequency, followed by Fe-17Mn(P) and the Fe-17Mn(U). The higher |Z| value corroborates the beneficial effect of chromium [10]. On the other hand, the lower values of |Z| in the prestressed Fe-17Mn may indicate that the initial stressed state of the surface influences the generation of the passive film, when it occurs naturally.

This image also corroborates that all the materials studied reach high impedance values at low frequencies, so it is considered that they generate stable passive layers at pH = 13, as well as showing the goodness of the fit.

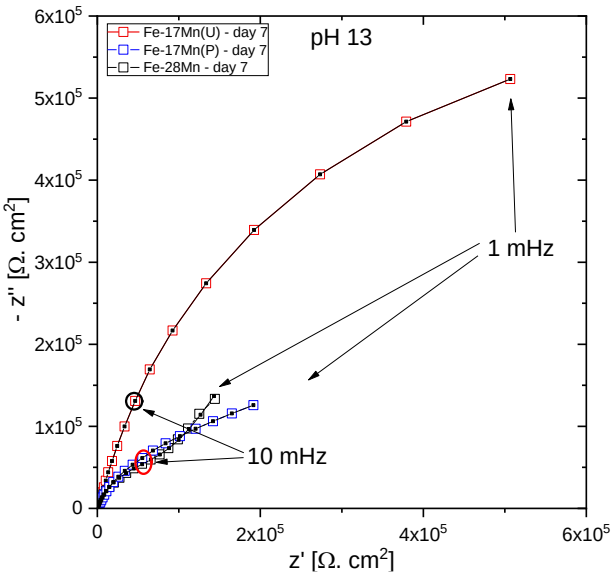


Figure 5: Nyquist diagram comparing the impedance values of the studied materials after 7 days of passivation in fresh concrete simulating solution (pH = 13), alongside the adjusted values.

The impedance spectra were modelled using electrical equivalent circuits. A 2RC circuit (Figure 6a) has been used for the Fe-17Mn(U) and for Fe-17Mn(P) and Fe-28Mn a 3RC circuit (Figure 6b) was used. In both circuits R_e Is interpreted as the electrolyte resistance and α as the depressed coefficient, affecting the capacitances.

In the 2RC circuit, the high frequency constant $R_1 \cdot C_1$ are interpreted as the charge transfer resistance and the double layer capacitance at the interface between the oxide layer and the electrolyte respectively. The low frequency constant, $R_2 \cdot C_2$, correlate to the redox processes taking place [45,46]

In the 3RC circuit, the first time constant, located at high frequencies, $R_1 \cdot C_1$, corresponds to the characteristics of the oxide film; the second time constant, located at intermediate frequencies, $R_2 \cdot C_2$, represents the double layer phenomenon and charge transfer at the metal-electrolyte interface; and the third time constant, located at lower frequencies, $R_3 \cdot C_3$, refers to the redox phenomena that take place in the oxide film, primarily associated with Fe.

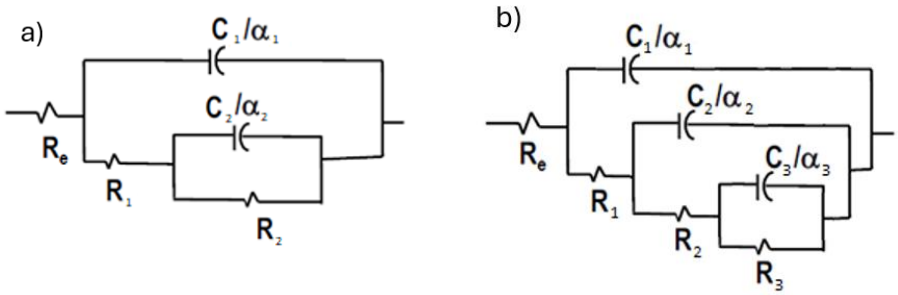


Figure 6: a) Cascaded 2RC and b) 3RC (right) equivalent circuits used for fitting experimental impedance data.

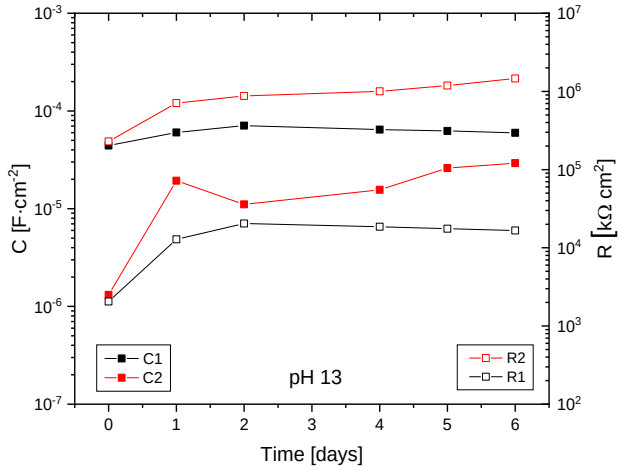


Figure 7 shows the high frequency constant values $R_1 \cdot C_1$ for Fe-17Mn(U) as the passive layer is generated and evolves. An increase of C_1 is initially observed, and it may be associated with the generation of metallic oxides.

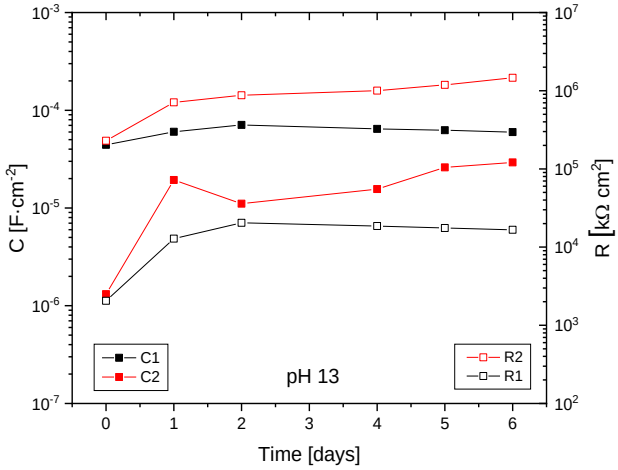


Figure 7 also shows the evolution of the low-frequency constant associated with the redox processes in the passive film. The evolution is characterized by a slight increase in both resistance and capacity during immersion time. The increase in resistance is expected and reflects the decrease in redox activity as the passive film stabilizes, even if the capacity also very slightly increases. Although the explanation is not clear the increase in the capacitance is probably related to the increase in the conductivity of the film.

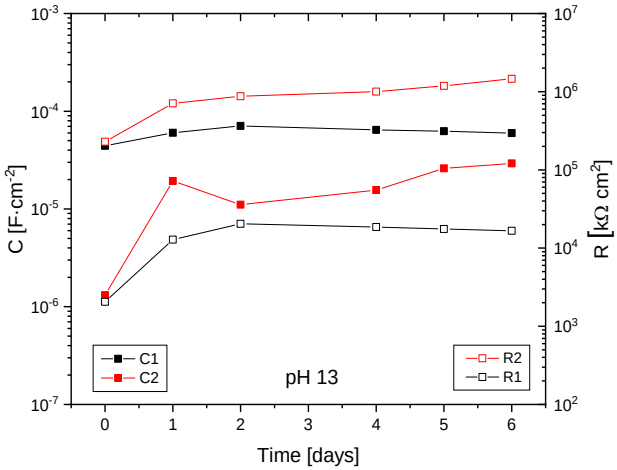


Figure 7: Evolution of the high frequency time constant (C_1, R_1) and the low frequency constant (C_2, R_2) with immersion time for the Fe-17Mn(U) in a 0.1M NaOH + 0.1M KOH solution, using the EEC represented in Figure 6a).

The impedance measurements made on the Fe-17Mn(P) and Fe-28Mn samples were modelled using the EEC shown in Figure 6b). In the case of Fe-28Mn, the measurements recorded at the beginning were modelled with the 2RC equivalent circuit, and after 24 hours of immersion, the 3RC circuit was used.

The evolution of the capacitance (Figure 8a) and resistance (Figure 8b) for the high, medium and low time constants is presented later in the document. The (C_1,R_1) values corresponding to the Fe-17Mn(U) are quite stable throughout the immersion time, confirming the generation of a stable film. A slight decrease in capacitance is observed, corresponding to the increase in film thickness. The resistance undergoes a slight increase in correspondence with the evolution of C_1.

In the case of Fe-28Mn, the evolution of C_1 is different. Excluding the first value, which refers not only to the characteristics of the film but also to the film/electrolyte interface, the values are very stable up to three days of immersion, where a sharp increase in capacity is observed, which can be related to a greater volume of oxides generated. Regarding the R_1 values, the general tendency is to decrease with immersion time, which indicates a greater ease of entry of the electrolyte into the film.

The film thickness developed under natural conditions was estimated using Eq. *6* [44], and assuming a value of 15.6 for the dielectric constant of the passive film oxides (ε_r)[47], and considering ε_0 as the vacuum permitivity ($8.85 \cdot 10^{-14}$ F·cm^{-1}) and A as the area of the electrode.

$$C_{dl} = \frac{\varepsilon_r \varepsilon_0 A}{d} \qquad \text{Eq. 6}$$

The thicknesses obtained were: 5.2 Å and 3.6 Å for the Fe-17Mn(P) and Fe-28Mn respectively. These values are slightly lower than those found in the literature [48], especially for Fe-28Mn. Although the reason is not clear, it is possible that, since these are semiconducting oxides, the contribution of the

charge space capacity within this C_1 must be taken into account, and that the calculated film thickness may be questionable.

Figure 8a and Figure 8b also show the evolution of the time constant at intermediate frequencies, (C_2, R_2), associated with the charge transfer resistance and the double layer capacitance at the oxide film/electrolyte interface. In general, the values do not change considerably during the immersion time, although a certain trend is observed, which varies depending on the material. In Fe-Mn(P), there is a slight increase in resistance, indicative of a slowdown in the oxidation process. This evolution does not correspond to the evolution of the capacitance, which also increases slightly, as observed in the Fe-17Mn(U) materials and which could be attributed to the semiconducting nature of the generated oxides. In Fe-28Mn both the resistance and capacitance decrease slightly, which may be associated with greater oxide generation.

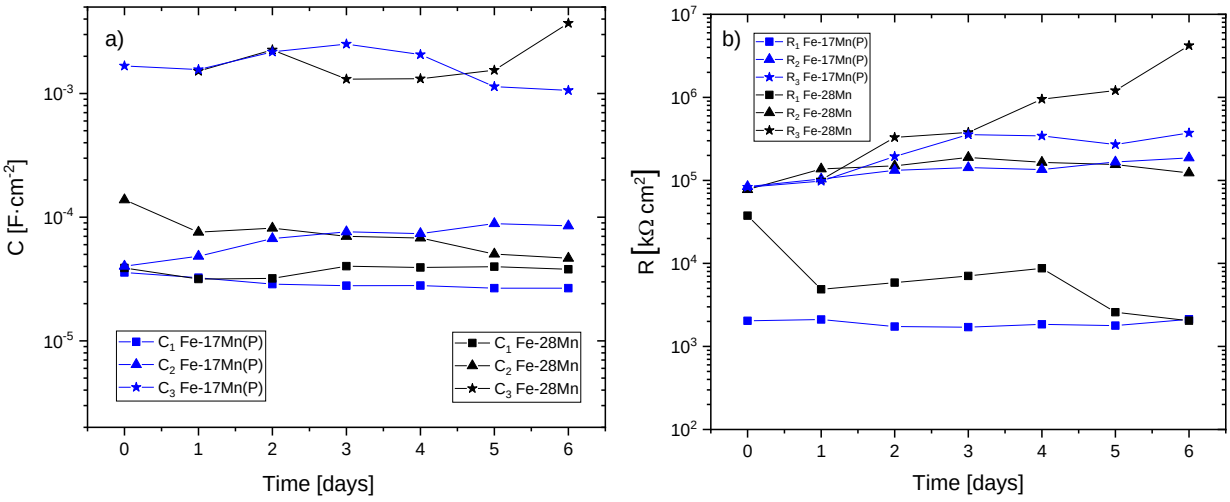


Figure 8: Evolution of the high-frequency time constant C_1 (a) R_1 (b) for the Fe-17Mn(P) and the Fe-28Mn with immersion time in a 0.1M NaOH + 0.1M KOH solution using the EEC shown in Figure 6b).

The evolution of the time constant at low frequencies, (C_3, R_3), (Figure 8a and Figure 8b) is associated with the redox processes of the materials. The most significant aspect is the evolution of the R_3 in both materials, which clearly increases with immersion time, corroborating the passivation process.

This study concludes that all the materials studied generate protective passive layers at this pH, although the kinetics of their generation and growth are very different. In Fe-28Mn, there are two film growth kinetics: a very brief initial stage with a very rapid rate, and a second in which the process slows down, resulting in stabilization times on the order of 7 days. The other systems have a single film growth rate, although the stabilization times are different, oscillating around 6 days for Fe-17Mn in both formats. Regarding the characteristics of the generated films, the highest impedances correspond to Fe-27Mn(U).

Previous studies carried out within the research group on the same Fe-based shape memory alloys under highly alkaline conditions (pH ≈ 13) and partially carbonated environments have provided a detailed characterization of the passive films formed on these materials. Cyclic voltammetry and X-ray photoelectron spectroscopy (XPS), including both general spectra and high-resolution analysis, revealed that the passive layers are mainly composed of Fe-, Mn- and Cr-based oxides, with differences in thickness and composition depending on the alloy and environmental conditions. In addition, Mott–Schottky analysis demonstrated that the passive films exhibit semiconducting behaviour, showing predominantly n-type characteristics in Fe-28Mn alloys, whereas a mixed n- and p-type behaviour was

observed in Fe-17Mn alloys due to the contribution of different oxide species. These results confirm that the electrochemical response of these alloys is governed by the nature and evolution of complex multilayer oxide films, supporting the interpretation of the impedance results obtained in the present work.

To assess the effect of the loss of environmental alkalinity on the passivation capacity of the steels under study, the ability of these materials to create passive layers was studied by monitoring the evolution of the potential with immersion time in a carbonated NaOH + KOH solution at a pH of 12.

During the passive layer generation process, the evolution of the OCP was monitored daily. Figure 9 shows the evolution of the OCP values of the steels. All the samples show passivity from the first measurement, that was taken after one hour of immersion in the solution, indicating that some surface passivation had already occurred. All OCPs show increasing values, remaining constant throughout the test in passivity regions, with Fe-28Mn showing the highest values. In general, the trends followed a similar pattern to that observed at pH = 13, with the most anodic potential values corresponds to the Fe-Mn steel with higher Mn and lower Cr contents.

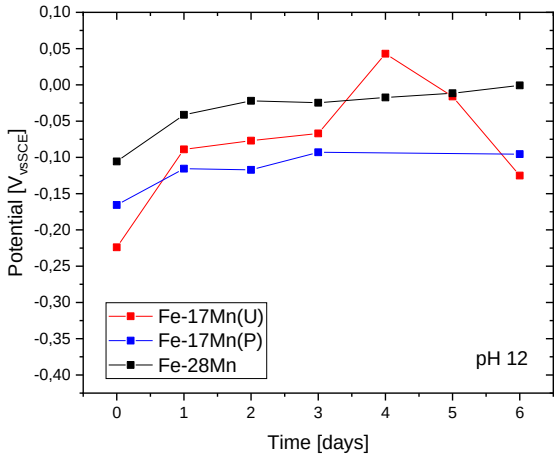


Figure 9: Evolution of the open circuit potential values of the studied materials with immersion time in a carbonated NaOH + KOH solution, with a pH = 12.

Figure 10 shows how the Fe-17Mn(U) sample exhibits an increasing |Z| with immersion time. Representative spectra are shown for clarity, while all measurements performed during the immersion period were used for the analysis of the impedance parameters. This increase is especially pronounced on the first day, remaining stable until with a slight decrease on day 6. This decrease coincides with the evolution of the OCP value, since in both cases the measured value decreases, although it does so while maintaining passivity parameters. The morphology of the phase angle represented in the Bode diagram (Figure 10b) suggests the presence of two-time constants.

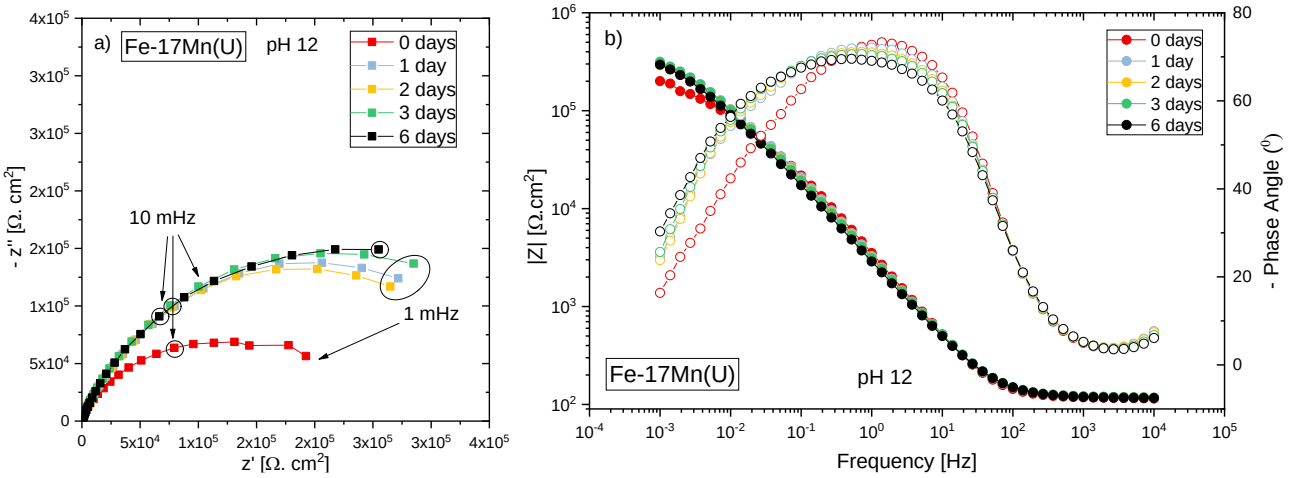


Figure 10: Evolution of the impedance values of Fe-17Mn(U) with immersion time in carbonated NaOH + KOH solution, with a pH = 12, Nyquist (a) and Bode (b) diagrams.

As can be seen in Figure 11 and like the previous example, the Fe-17Mn(P) sample experiences an increase in the |Z| value due to the generation of the passive layer. In this material, the phase angle morphology is different, presenting a single wide relative maximum on day 0 and two relative maxima after day 1. This phenomenon is due to the separation of the two time constants, located at medium frequencies.

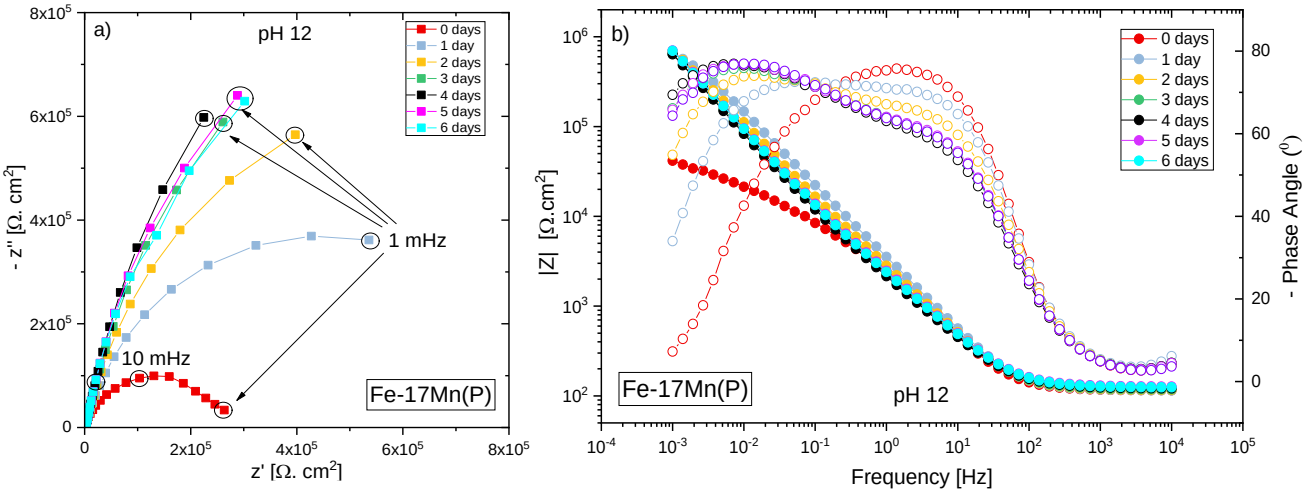


Figure 11: Evolution of the impedance values of Fe-17Mn(P) after being immersed in carbonated NaOH + KOH solution, with a pH = 12 for 7 days, Nyquist (a) and Bode (b) diagrams.

In Figure 12b, Fe-28Mn shows an increase in the |Z| value associated with the generation and growth of the passive film, which is consistent with the evolution of the OCP. Also, as in the other systems, it is possible to distinguish two time constants, although less distinct than in the case of Fe-17Mn(P). After studying the evolution of the passive layers of the materials in a pH =12 solution, it can be concluded that all the shape memory steels generate protective passive layers at this pH value.

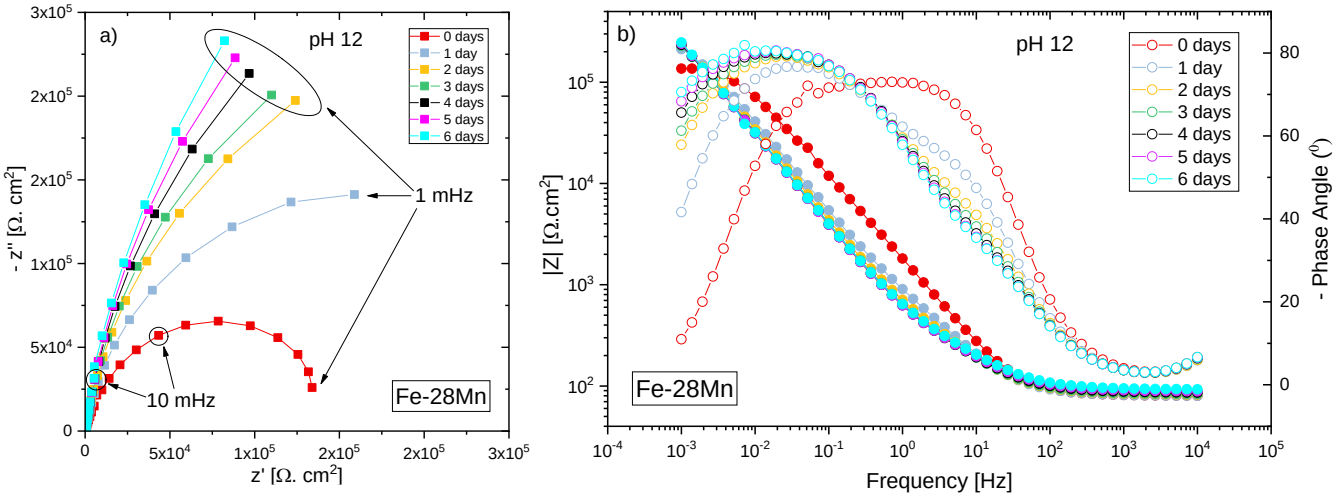


Figure 12: Evolution of the impedance values of Fe-28Mn after being immersed in a carbonated NaOH + KOH solution with pH = 12 for 7 days, represented in the Nyquist (a) and Bode (b) diagrams.

To assess the ability of the materials under study to generate passive layers in environments with lower alkalinity levels, their behavior is studied after being immersed in a solution with a pH = 11, composed of 0.1 M NaOH + 0.1 M KOH and carbonated using the CO_2 bubbling method. Figure 13 shows the results of the open-circuit potential monitoring recorded during the test. For all materials, the OCP values remained within the passivity range throughout the study period, with increasing trends for all materials except Fe-17Mn(U), although even in this material the OCP values corresponds to a passive state.

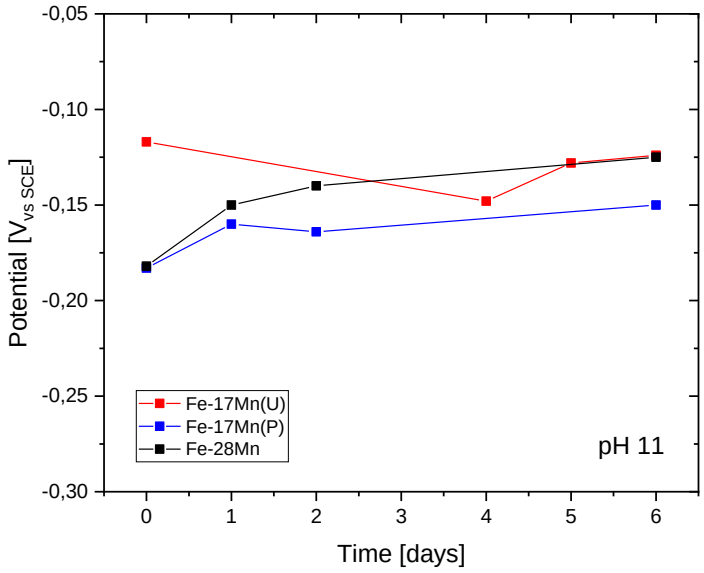


Figure 13: Evolution of the OCP values of studied materials exposed to a carbonated NaOH + KOH solution at pH = 11.

The impedance evolution of Fe-17Mn(U) with immersion time is shown in Figure 14. Only some data is presented to avoid excessive overlaying. As can be seen, it was different to what was observed at higher pH values. The impedance values are lower and no increase in impedance is observed with immersion time. Even some decrease is observed, which may indicate some dissolution of the film. In any case, the high impedance values together with the recorded potentials (around -120 $mV_{vs\ SCE}$) point to the formation of a passive layer, perhaps with a lesser quality than in more alkaline environments.

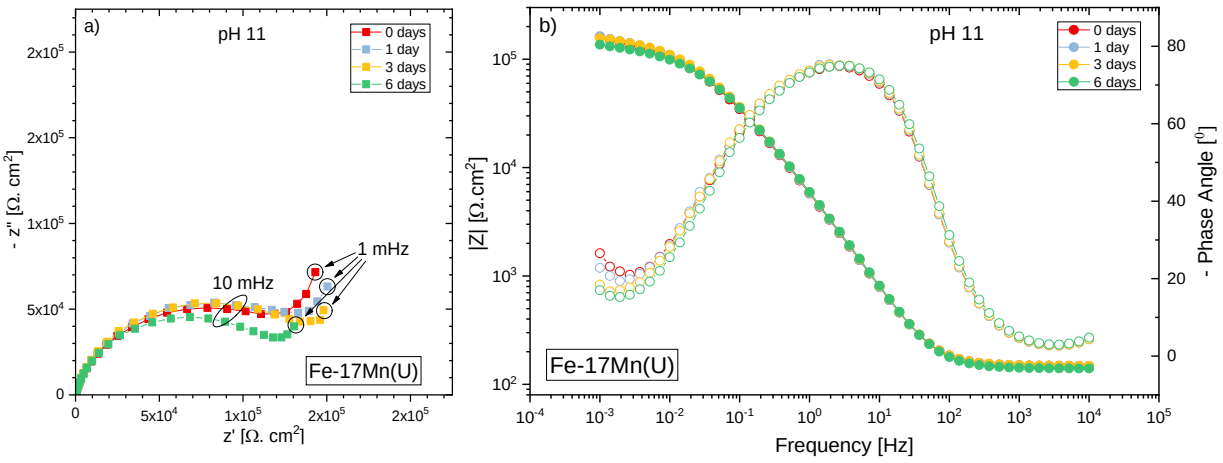


Figure 14: Evolution of the impedance values of Fe-17Mn(U) after being immersed in NaOH + KOH solution, with a pH = 11 for 7 days, Nyquist (a) and Bode (b) diagrams.

Figure 15 shows the impedance evolution of Fe-17Mn(P) at pH = 11. The sharp decrease observed in the impedance after 24 hours of immersion is striking, suggesting that the formation of a passive film is very quickly and after that, it experiences a thinning. The impedance reaches stable values only slightly lower than those observed for Fe-17Mn(U) after 24 hours of immersion. Therefore, again, the recorded potential values (approximately -150 $mV_{vs.SCE}$) as well as the stability of the impedance measurements corroborate the passivation of Fe-17Mn(P), although it seems that the generated film is less protective than in the case of Fe-17Mn(U) in the pH = 11 solution.

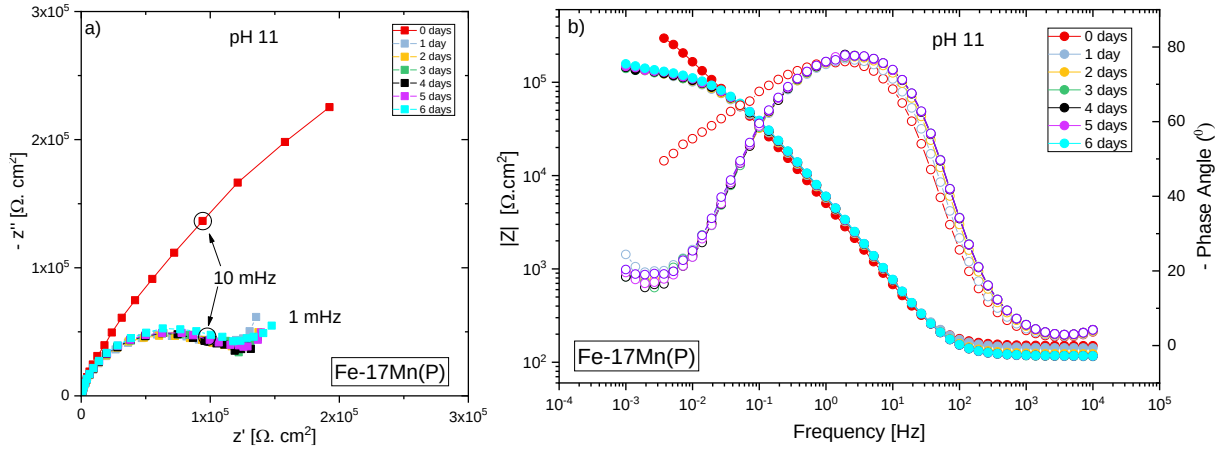


Figure 15: Evolution of the impedance values of Fe-17Mn(P) after being immersed in NaOH + KOH solution, with a pH = 11 for 7 days, Nyquist (a) and Bode (b) diagrams.

The evolution of Fe-28Mn at pH = 11 is shown in Figure 16. As in the case of Fe-17Mn(U), the |Z| values are very similar throughout the immersion period, especially the high-frequency arc, with a diameter that was practically constant over the 7 days of immersion. If this arc is considered to correspond to the film's response, the results obtained suggest the existence of a stable film, at least during the immersion period tested.

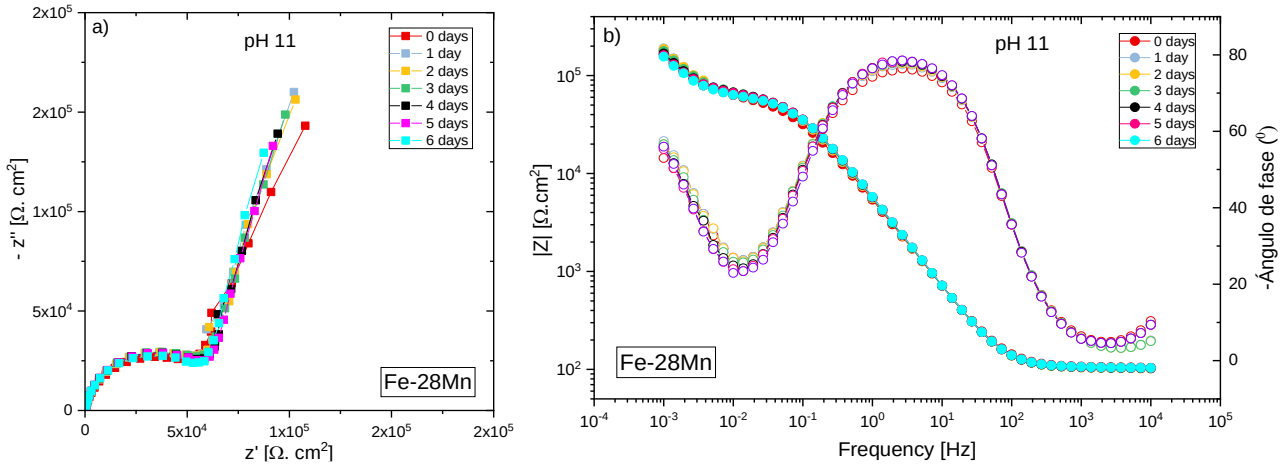


Figure 16: Evolution of the impedance values of Fe-28Mn with immersion time in a NaOH + KOH solution, with a pH = 11, Nyquist (a) and Bode (b) diagrams.

After studying the evolution of the OCP and impedance values of both SMS, it can be deduced that a passive film also forms on these samples at this pH. The |Z| values are slightly lower than those obtained at pH 13 or pH 12, suggesting a less protective effect. Furthermore, the film forms at the beginning of immersion and remains virtually unchanged over the 7-day test period, the only exception is Fe-17Mn(P) in which it seems that certain thinning occurs after 24 hours of immersion.

4. Conclusions

An electrochemical study of 2 different alloys, Fe-28Mn-6Si-5Cr and Fe-17Mn-10Cr-5Si-4Ni-1(V,C), was performed using OCP monitoring as well as EIS, in alkaline environments simulating concrete pore solutions with decreasing pH. The following conclusions were obtained:

- Both samples of the Fe-17Mn alloy (untreated and prestressed) as well as the Fe-28Mn steelshow spontaneous passivation when subjected to pH = 13 conditions, reflected in the increase of the OCP value, as well in the increased impedance modulus obtained in the EIS study. Those results confirm the ability of both alloys to create passive films in concrete-like pH.
- The kinetics of the passive layer formation and growth are significantly different in both alloys, which is clearly seen in the OCP evolution. The stabilization time calculated from the OCP evolution was approximately **181 h for Fe-28Mn**, whereas values of **157.8 h and 143.1 h** were obtained for Fe-17Mn(U) and Fe-17Mn(P), respectively
- EEC modelling of the EIS results, using both 2RC and 3RC values, show increases in the resistance values (R_1 - R_3), consistent with the passive layer growth in all 3 alloys.
- The three types of samples show signs of passivation when immersed in a pH = 12 solution, although the |Z| values suggest a lower passivity than that developed in a pH = 13 solution.
- When immersed in a pH = 11 solution the samples present notably lower impedance values, with lower impedance modulus values and a limited growth within the tested immersion time. This behaviour suggests a reduced ability to form passive layers for all the shape memory alloys in the tested conditions as well as a very limited oxide film growth under partially carbonated concrete conditions

5. References

[1] F.C. Nascimento Borges, Iron Based Shape Memory Alloys: Mechanical and Structural Properties, Shape Memory Alloys - Processing, Characterization and Applications (2013). https://doi.org/10.5772/51877.

[2] A. Sato, E. Chishima, K. Soma, T. Mori, Shape memory effect in γ⇄ϵ transformation in Fe-30Mn-1Si alloy single crystals, Acta Metallurgica 30 (1982) 1177–1183. https://doi.org/10.1016/0001-6160(82)90011-6.

[3] A. Cladera, B. Weber, C. Leinenbach, C. Czaderski, M. Shahverdi, M. Motavalli, Iron-based shape memory alloys for civil engineering structures: An overview, Constr. Build. Mater. 63 (2014) 281–293. https://doi.org/10.1016/j.conbuildmat.2014.04.032.

[4] L. Janke, C. Czaderski, M. Motavalli, J. Ruth, Applications of shape memory alloys in civil engineering structures - Overview, limits and new ideas, Materials and Structures/Materiaux et Constructions 38 (2005) 578–592. https://doi.org/10.1617/14323.

[5] A. Druker, P. Vermaut, J. Malarría, The shape recovery conditions for Fe–Mn–Si alloys: An interplay between martensitic transformation and plasticity, Mater. Charact. 139 (2018) 319–327. https://doi.org/10.1016/j.matchar.2018.03.018.

[6] I. Nikulin, T. Sawaguchi, K. Ogawa, K. Tsuzaki, Effect of γ to ε martensitic transformation on low-cycle fatigue behaviour and fatigue microstructure of Fe-15Mn-10Cr-8Ni-xSi austenitic alloys, Acta Mater. 105 (2016) 207–218. https://doi.org/10.1016/j.actamat.2015.12.002.

[7] T. Maruyama, T. Kurita, S. Kozaki, K. Andou, S. Farjami, H. Kubo, Innovation in producing crane rail fishplate using Fe-Mn-Si-Cr based shape memory alloy, Materials Science and Technology 24 (2008) 908–912. https://doi.org/10.1179/174328408X302585.

[8] K.K. Jee, J.H. Han, W.Y. Jang, A method of pipe joining using shape memory alloys, Materials Science and Engineering: A 438–440 (2006) 1110–1112. https://doi.org/10.1016/j.msea.2006.02.094.

[9] B. Cao, T. Iwamoto, A strength prediction of joints by Fe-Mn-Si-Cr shape memory alloy through strain monitoring during pre-processes including diameter expansion and tightening by heating, Eng. Fract. Mech. 284 (2023) 109234. https://doi.org/10.1016/j.engfracmech.2023.109234.

[10] D. Dias, S. Nakamatsu, C.A. Della Rovere, J. Otubo, N.A. Mariano, Characterization and Corrosion Resistance Behavior of Shape Memory Stainless Steel Developed by Alternate Routes, Metals (Basel). 10 (2019) 13. https://doi.org/10.3390/met10010013.

[11] B. Schranz, J. Michels, M. Shahverdi, C. Czaderski, Strengthening of concrete structures with iron-based shape memory alloy elements: Case studies, SMAR 2019 - Fifth Conference on Smart Monitoring, Assessment and Rehabilitation of Civil Structures (2019) 1–8.

[12] J.Y. Lee, J.S. Hong, S.H. Kang, Y.K. Lee, The effect of austenite grain size on deformation mechanism of Fe–17Mn steel, Materials Science and Engineering: A 809 (2021). https://doi.org/10.1016/j.msea.2021.140972.

[13] M. Vollmer, A. Bauer, J.M. Frenck, P. Krooß, A. Wetzel, B. Middendorf, E. Fehling, T. Niendorf, Novel prestressing applications in civil engineering structures enabled by

Fe[sbnd]Mn[sbnd]Al[sbnd]Ni shape memory alloys, Eng. Struct. 241 (2021). https://doi.org/10.1016/j.engstruct.2021.112430.

[14] S. Zareie, A.S. Issa, R.J. Seethaler, A. Zabihollah, Recent advances in the applications of shape memory alloys in civil infrastructures: A review, Structures 27 (2020) 1535–1550. https://doi.org/10.1016/j.istruc.2020.05.058.

[15] G.C. Lecis, C. Lenardi, A. Sabatini, The Effect of Mn-Depleted Surface Layer on the Corrosion Resistance of Shape Memory Fe-Mn-Si-Cr Alloys, 1997. https://doi.org/https://doi.org/10.1007/s11661-997-0287-z.

[16] O. Söderberg, X.W. Liu, P.G. Yakovenko, K. Ullakko, V.K. Lindroos, Corrosion behaviour of Fe-Mn-Si based shape memory steels trained by cold rolling, Materials Science and Engineering A 273–275 (1999) 543–548. https://doi.org/10.1016/S0921-5093(99)00396-2.

[17] Y.S. Zhang, X.M. Zhu, Electrochemical polarization and passive film analysis of austenitic Fe-Mn-Al steels in aqueous solutions, Corros. Sci. 41 (1999) 1817–1833. https://doi.org/10.1016/S0010-938X(99)00017-7.

[18] Z.X. Ye, M. Zhu, W. Lan, Y.F. Yuan, Enhanced anti-corrosion performance and hardness of FeCoNi medium entropy alloys via deep cryogenic treatment and cyclic deep cryogenic treatment, Mater. Chem. Phys. 348 (2026). https://doi.org/10.1016/j.matchemphys.2025.131742.

[19] Z.X. Ye, M. Zhu, Y.F. Yuan, Research on the Enhanced Corrosion Resistance of FeCoNi Medium Entropy Alloy in Simulated Seawater Containing NO3−, J. Mater. Eng. Perform. (2025). https://doi.org/10.1007/s11665-025-12946-0.

[20] X.M. Zhu, Y.S. Zhang, Investigation of the Electrochemical Corrosion Behavior and Passive Film for Fe-Mn, Fe-Mn-Al, and Fe-Mn-Al-Cr Alloys in Aqueous Solutions, Corrosion 54 (1998) 3–12. TI-6AL

[21] Y.S. Zhang, X.M. Zhu, M. Liu, R.X. Che, Effects of anodic passivation on the constitution, stability and resistance to corrosion of passive film formed on an Fe-24Mn-4Al-5Cr alloy, Appl. Surf. Sci. 222 (2004) 89–101. https://doi.org/10.1016/j.apsusc.2003.08.068.

[22] C.A.D. Rovere, J.H. Alano, J. Otubo, S.E. Kuri, Corrosion behavior of shape memory stainless steel in acid media, J. Alloys Compd. 509 (2011) 5376–5380. https://doi.org/10.1016/j.jallcom.2011.02.051.

[23] H.C. Lin, K.M. Lin, C.S. Lin, T.M. Ouyang, The corrosion behavior of Fe-based shape memory alloys, Corros. Sci. 44 (2002) 2013–2026. https://doi.org/10.1016/S0010-938X(02)00027-6.

[24] C.A. Della Rovere, J.H. Alano, R. Silva, P.A.P. Nascente, J. Otubo, S.E. Kuri, Characterization of passive films on shape memory stainless steels, Corros. Sci. 57 (2012) 154–161. https://doi.org/10.1016/j.corsci.2011.12.022.

[25] W.J. Lee, R. Partovi-Nia, T. Suter, C. Leinenbach, Electrochemical characterization and corrosion behavior of an Fe-Mn-Si shape memory alloy in simulated concrete pore solutions, Materials and Corrosion 67 (2016) 839–846. https://doi.org/10.1002/maco.201508701.

[26] J. Joo, M. Kang, D. Shin, E. Seo, D. Kim, Y. Yeon, K. Hong, W. Lee, J. Lee, Corrosion resistance of shape recoverable fe-17mn-5si-5cr alloy in concrete structures, Materials 13 (2020) 1–11. https://doi.org/10.3390/ma13235531.

[27] K.L. Lou, M. Zhu, Y.F. Yuan, L. Nie, Degradation of Anti-Corrosion Performance of TC4 Alloy under the Synergistic Impacts of F− Ion and Alternating Current in Simulated Seawater, J. Mater. Eng. Perform. (2025). https://doi.org/10.1007/s11665-025-12964-y.

[28] K.L. Lou, M. Zhu, Y.F. Yuan, Corrosion characteristic of Ti-6Al-4V alloy imposed with AC interference in simulated seawater containing thiosulfate, Mater. Today Commun. 50 (2026). https://doi.org/10.1016/j.mtcomm.2025.114571.

[29] J.M. Frenck, J. Link, M. Vollmer, T. Niendorf, Electrochemical characterization of Fe-Mn-Al-Ni shape memory alloy in an alkaline solution contaminated with Cl- ions, Mater. Lett. 346 (2023). https://doi.org/10.1016/j.matlet.2023.134457.

[30] A. Collazo, R. Figueroa, C. Mariño-Martínez, X.R. Nóvoa, C. Pérez, Electrochemical characterization of a Fe-based shape memory alloy in an alkaline medium and the behaviour in aggressive conditions, Electrochim. Acta 444 (2023). https://doi.org/10.1016/j.electacta.2023.142034.

[31] A. Sato, E. Chishima, K. Soma, T. Mori, Shape memory effect in γ⇄ϵ transformation in Fe-30Mn-1Si alloy single crystals, Acta Metallurgica 30 (1982) 1177–1183. https://doi.org/10.1016/0001-6160(82)90011-6.

[32] L. Janke, Applications of shape memory alloys in civil engineering structures - Overview, limits and new ideas, Mater. Struct. 38 (2005) 578–592. https://doi.org/10.1617/14323.

[33] T. Maruyama, T. Kurita, S. Kozaki, K. Andou, S. Farjami, H. Kubo, Innovation in producing crane rail fishplate using Fe–Mn–Si–Cr based shape memory alloy, Materials Science and Technology 24 (2008) 908–912. https://doi.org/10.1179/174328408X302585.

[34] D. Dias, S. Nakamatsu, C.A. Della Rovere, J. Otubo, N.A. Mariano, Characterization and Corrosion Resistance Behavior of Shape Memory Stainless Steel Developed by Alternate Routes, Metals (Basel). 10 (2019) 13. https://doi.org/10.3390/met10010013.

[35] J.Y. Lee, J.S. Hong, S.H. Kang, Y.K. Lee, The effect of austenite grain size on deformation mechanism of Fe–17Mn steel, Materials Science and Engineering: A 809 (2021). https://doi.org/10.1016/j.msea.2021.140972.

[36] Y.S. Zhang, X.M. Zhu, M. Liu, R.X. Che, Effects of anodic passivation on the constitution, stability and resistance to corrosion of passive film formed on an Fe-24Mn-4Al-5Cr alloy, Appl. Surf. Sci. 222 (2004) 89–101. https://doi.org/10.1016/j.apsusc.2003.08.068.

[37] C.A. Della Rovere, J.H. Alano, J. Otubo, S.E. Kuri, Corrosion behavior of shape memory stainless steel in acid media, J. Alloys Compd. 509 (2011) 5376–5380. https://doi.org/10.1016/j.jallcom.2011.02.051.

[38] H.C. Lin, K.M. Lin, C.S. Lin, T.M. Ouyang, The corrosion behavior of Fe-based shape memory alloys, Corros. Sci. 44 (2002) 2013–2026. https://doi.org/10.1016/S0010-938X(02)00027-6.

[39] J. Joo, M. Kang, D. Shin, E. Seo, D. Kim, Y. Yeon, K. Hong, W. Lee, J. Lee, Corrosion resistance of shape recoverable Fe-17Mn-5Si-5Cr alloy in concrete structures, Materials 13 (2020) 1–11. https://doi.org/10.3390/ma13235531.

[40] O. Matsumura, S. Furusako, T. Sumi, T. Furukawa, H. Otsuka, Improvement of shape memory effect due to low-finishing-temperature hot-rolling in an Fe–28Mn–6Si–5Cr alloy, Materials

Science and Engineering: A 272 (1999) 459–462. https://doi.org/10.1016/S0921-5093(99)00480-3.

[41] C. Leinenbach, H. Kramer, C. Bernhard, D. Eifler, Thermo-Mechanical Properties of an Fe-Mn-Si-Cr-Ni-VC Shape Memory Alloy with Low Transformation Temperature, Adv. Eng. Mater. 14 (2012) 62–67. https://doi.org/10.1002/adem.201100129.

[42] J.A. Nelder, R. Mead, A Simplex Method for Function Minimization, Comput. J. 7 (1965) 308–313. https://doi.org/10.1093/comjnl/7.4.308.

[43] D.D. Macdonald, Passivity. The key to our metals-based civilization, 1999.

[44] C. Mariño-Martínez, A. Collazo, R. Figueroa, X.R. Nóvoa, C. Pérez, Investigation of the electrochemical behaviour of Fe-28Mn-6Si-5Cr shape memory alloy in alkaline media, Constr. Build. Mater. 471 (2025) 140680. https://doi.org/10.1016/j.conbuildmat.2025.140680.

[45] B. Messaoudi, S. Joiret, M. Keddam, H. Takenouti, Anodic behaviour of manganese in alkaline medium, Electrochim. Acta 46 (2001) 2487–2498. https://doi.org/10.1016/S0013-4686(01)00449-2.

[46] C.M. Abreu, M.J. Cristóbal, R. Losada, X.R. Nóvoa, G. Pena, M.C. Pérez, Long-term behaviour of AISI 304L passive layer in chloride containing medium, Electrochim. Acta 51 (2006) 1881–1890. https://doi.org/10.1016/j.electacta.2005.06.040.

[47] R. Babić, M. Metikoš-Huković, Semiconducting properties of passive films on AISI 304 and 316 stainless steels, Journal of Electroanalytical Chemistry 358 (1993) 143–160. https://doi.org/10.1016/0022-0728(93)80435-K.

[48] Y.-M. Chen, N.G. Rudawski, E. Lambers, M.E. Orazem, Application of Impedance Spectroscopy and Surface Analysis to Obtain Oxide Film Thickness, J. Electrochem. Soc. 164 (2017) C563–C573. https://doi.org/10.1149/2.1061709jes.

6. Funding

Not applicable.

7. Conflict of interests

On behalf of all authors, the corresponding author states that there is no conflict of interest.

8. Data Availability Statements

Not applicable.